Extreme Mechanics Letters 39 (2020) 100837

Contents lists available at ScienceDirect

Extreme Mechanics Letters

journal homepage: www.elsevier.com/locate/eml

Shaping elastic wave mode conversion with a piezoelectric-based programmable meta-boundary

Xiaopeng Li [a], Yangyang Chen [a,*], Xiaodong Zhang [a,b], Guoliang Huang [a,*]

[a] Department of Mechanical and Aerospace Engineering, University of Missouri, Columbia, MO 65211, USA
[b] State Key Laboratory of Advanced Design and Manufacturing for Vehicle Body, Hunan University, 410082 Changsha, People's Republic of China

ARTICLE INFO

Article history:
Received 14 February 2020
Received in revised form 5 June 2020
Accepted 5 June 2020
Available online 12 June 2020

Keywords:
Elastic wave mode-conversion
Programmability
Meta-boundary

ABSTRACT

Pressure-shear wave conversions on free boundaries or interfaces of solids are peculiar and unavoidable wave phenomena in two-dimensional (2D) elasticity, compared with electromagnetic and acoustic wave systems. However, flexibly tailoring their conversions in a reversible and programmable manner to meet a predefined conversion efficiency and spatial distributions of converted wave fields has never been touched before. In this letter, we introduce a programmable meta-boundary with deep subwavelength thickness that is composed of an array of piezoelectric sensing-and-actuating units controlled by electrical circuits such that pressure to shear wave conversions are able to be electrically reconfigured. Through numerical simulations, we show the meta-boundary can nearly totally convert an incident pressure wave to a reflected shear wave even for normal incidences. Thanks to the programmability of electrical control circuits, incident waves can span a large range of angles, from negative to positive values, and reflected shear waves converted from pressure waves are also able to be steered to different directions. The design could find potential applications in protection of underwater structures, acoustic cloaks, ultrasonic imaging and new types of shear-wave-transducer devices.

1. Introduction

Two dimensional isotropic solids usually support two orthogonal bulk wave modes: dilatational/pressure (P-) and distortional/shear (S-) waves [1]. They can be coupled with each other in the presence of discontinuities [1]. Wave mode conversions are peculiar wave phenomena associated with these couplings. They have been characterized by Snell's law when interfaces or boundaries are flat. For some applications, such as elastic wave lenses, energy harvesting and sometimes in structural health monitoring and nondestructive evaluation, elastic wave mode conversions need to be kept minimum [2–4]. Whereas, there exists several scenarios where elastic wave mode conversions are expected to be maximum, such as protection of underwater structures, acoustic cloaks, ultrasonic imaging and new types of shear-wave-transducer designs [4–11]. Driven by those motivation, manipulating elastic wave mode conversion has long been pursued, especially when the concept of mechanical metamaterials/metasurfaces have been suggested recently [12–15]. For example, double-negative metamaterials [12], Fabry–Pérot resonant metasurface [13] and transmodal metasurface [15] have displayed mode conversions between P- and S-waves. However, finding an approach that can flexibly shape elastic wave conversions in a reversible and programmable way to accomplish a predefined conversion efficiency and spacial distributions of converted wave fields is still a challenge topic.

Active/reconfigurable/programmable mechanical metamaterials and metasurfaces have demonstrated their potentials for achieving tunable and controllable material properties and functionalities in both static and dynamic regimes [16–22]. They are typically designed by implementing active/smart material elements into passive metamaterial microstructures [18,23], i.e. by using smart polymers [16,18], liquid metals [24,25], shape memory materials [26] and photosensitive materials [27]. Nevertheless, those soft materials usually display relatively large material damping, which prevents them from linear elastodynamic applications. On the other hand, the piezoelectric shunt technique, which although usually contains feedback control loops and is much more complex, has proved as an efficient and highly flexible approach for elastic wave and vibration control [22,28,29]. Aligned with this technology, it has been demonstrated numerous interesting and superior properties and functionalities, ranging from real-time tunability [22,30], broadband operability [22,31,32], and multifunctionality [22,33,34] beyond passive counterparts.

* Corresponding authors.
E-mail addresses: yc896@missouri.edu (Y. Chen), huangg@missouri.edu (G. Huang).

https://doi.org/10.1016/j.eml.2020.100837
2352-4316/

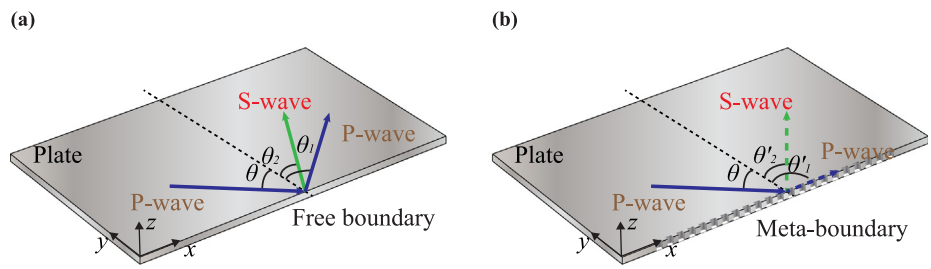

Fig. 1. (a) Elastic wave mode conversion on a free boundary; (b) Elastic wave mode conversion on a piezoelectric-based programmable meta-boundary.

In this letter, we aim to design a piezoelectric-based programmable meta-boundary on a thin elastic plate that can manipulate P- to S-wave mode conversions by reconfiguring electrical control circuits. The programmable meta-boundary is composed of an array of piezoelectric sensing-and-actuating units connected by electrical control circuits. We analytically derive P- to S-wave mode conversion relations in terms of the phase gradient of reflection coefficients on a boundary. In a one-dimensional (1D) setting, we bridge connections between reflection coefficient of longitudinal waves and corresponding transfer functions implemented in the control system. Through numerical simulations, we validate the design and show the meta-boundary can nearly totally convert an incident P-wave to a reflected S-wave even for normal incidence. The programmability of electrical control circuits allows incident waves to span a large range of angles and reflected shear waves to be steered to different directions. The programmable meta-boundary is expected to prompt device development in protection of underwater infrastructures, ultrasonic imaging and new transducers for shear wave generations.

2. Design of the meta-boundary for controlling wave mode conversions

2.1. Phase-gradient meta-boundary

Let us first consider elastic wave reflections on free boundaries of a thin elastic rectangular plate (Fig. 1a). We mainly focus on P-wave incidence in this study. When a plane P-wave is incident to one of its free boundaries at the angle, θ, the P-wave is directly reflected back at the angle, $\theta_1 = \theta$. At the same time, a plane S-wave is also generated and reflected back at the angle θ_2, due to the continuity conditions. The relations between incident and reflected angles are followed by Snell's law [1],

$$k_p \sin(\theta) = k_p \sin(\theta_1) = k_s \sin(\theta_2), \tag{1}$$

where k_p and k_s denote wavenumbers of P- and S-waves, respectively. The amplitude ratio between reflected and incident waves is predetermined when the material and incident angle are defined. It has been shown that this ratio tends to be extremely small when θ becomes small [1]. Inspired by the trans-modal metasurface [15], introducing phase-gradient on local reflection coefficients only for P-waves can effectively modify not only the relations between incident and reflected angles imposed by Snell's law (Eq. (1)) but also their amplitude ratios. The generalized Snell's law then reads [15]

$$k_p \sin(\theta) + \frac{\Delta\phi}{\Delta x} = k_p \sin(\theta_1') = k_s \sin(\theta_2'), \tag{2}$$

where $\frac{\Delta\phi}{\Delta x}$ represents the phase gradient of local reflection coefficients of P-waves along x-direction, and θ_1' and θ_2' denote reflected angles of P- and S-waves, respectively (Fig. 1b). As indicated in Eq. (2), the term, $\frac{\Delta\phi}{\Delta x}$, allows for tailoring angles, θ_1' and θ_2' to different values other than that constrained by Eq. (1). Once reflected angles are changed, the amplitude ratios between reflected P- and S-waves can also be modified. Our particular attention in the next section, however, is paid on the cases, where $\sin(\theta) + \frac{1}{k_p}\frac{\Delta\phi}{\Delta x} > 1$ (or $\sin(\theta) + \frac{1}{k_p}\frac{\Delta\phi}{\Delta x} < -1$), while $0 < \frac{k_p}{k_s}\sin(\theta) + \frac{1}{k_s}\frac{\Delta\phi}{\Delta x} < 1$ (or $-1 < \frac{k_p}{k_s}\sin(\theta) + \frac{1}{k_s}\frac{\Delta\phi}{\Delta x} < 0$). This is possible, when $k_p < k_s$, and material parameters of most of isotropic materials satisfy this condition. For those cases, reflected P-waves will become evanescent, as $\sin(\theta_1') > 1$ (or $\sin(\theta_1') < -1$), and only reflected S-waves are retained. Therefore, incident P-waves can be totally converted to S-waves. To achieve this wave phenomenon, a meta-boundary unit cell that can be easily programmed to realize on demand phase profiles of reflected P-waves will be introduced in the followings.

2.2. Design of piezoelectric-based programmable meta-boundary

To construct the piezoelectric-based programmable meta-boundary, an array of short rods at a portion of a boundary is firstly cut from a host plate (Fig. 2a). Incident P-waves can be converted to longitudinal and transverse waves propagating along the 1D short rods, when $\theta \neq 0$. In the following microstructural design, we aim to manipulate phases of reflected longitudinal waves and leave transverse waves intact. The length of the short rods is designed at an extremely subwavelength scale such that the P- and S-wave conversion at the plate boundary can still be approximated by Eq. (2). For the purpose of the phase manipulation, we attach one piezoelectric patch on each tip of those rods to function as actuator (Fig. 2a). When applying voltage signals, longitudinal waves will be generated and propagate through the rod. Thanks to constructive and/or destructive interference with the reflected longitudinal wave at that end boundary, the phase and magnitude of the reflection coefficient of longitudinal waves can be flexibly tailored. To automatically determine when and how to apply voltage signals to those actuators, we implement a feedback control loop. A piezoelectric sensor is bonded on a thin beam and finally attached to the surface of the actuator (Fig. 2a), such that longitudinal wave signals are effectively detected thanks to the resonant motion of this thin beam. Specifically, a charge amplifier that converts electrical charges to voltage signals is connected to the sensor. The sensing signal, V_s, is fed to a controller. The output voltage signal from the controller is amplified by a voltage amplifier to V_a and finally applied to the actuator. The relations between sensing and actuating signals are defined by a transfer function, $H = V_a/V_s$. In the design, sensing signals contain components from incident, reflected and actuator-generated longitudinal waves, making the system feedback. In order to conduct future experimental testing, two main issues must be addressed: (1) the electrical transfer function in time-domain should be properly designed to be causal, scalable and stable; (2) the meta-boundary should be fabricated with high precision to avoid the coupling with asymmetric wave modes.

We develop an analytical model to determine the transfer function, H, for achieving a desired local phase modulation. Wave

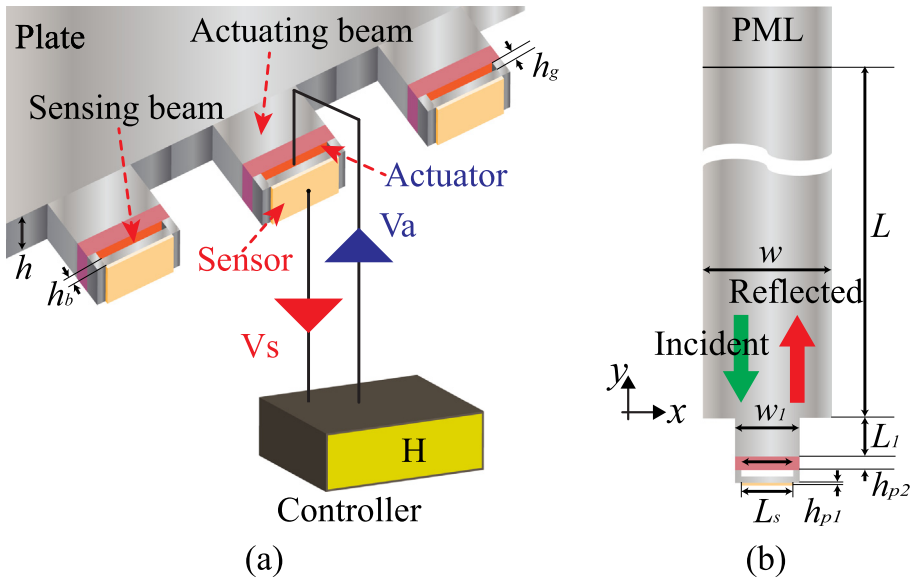

Fig. 2. (a) Design of the piezoelectric-based programmable meta-boundary; (b) Schematic of the one-dimensional setting of the meta-boundary unit cell.

propagation is considered on a 1D rod with a meta-boundary unit cell on the free end (Fig. 2b). Periodic boundary conditions are applied on the left and right edges of the rod. The width of the rod is selected as the periodicity, w, of the two-dimensional plate implemented with the meta-boundary. The length and width of the short rod in the meta-boundary are denoted as L_1 and w_1, respectively, and the thicknesses of the resonant sensing beam is represented by h_b. The gap between the actuator and the sensing beam is denoted as h_g. The thicknesses of the sensor and actuator are represented by h_{p1} and h_{p2}, respectively, and L_s denotes the length of the sensor. Consider an incident P-wave in Fig. 2b, of which the displacement field can be simply written as

$$u_i = U_0 e^{-ik_p y} \tag{3}$$

where U_0 denotes the complex wave amplitude of the incident wave. The time harmonic term, $e^{-i\omega t}$, is suppressed from Eq. (3), which is also applied throughout the rest of this study. In the absence of V_a, the reflected wave field at the free boundary can be approximately described by

$$u_r^{(p)} = U_0 e^{ik_p y} \tag{4}$$

Note that Eq. (4) is valid, when the length of the short rod in the meta-boundary is much smaller than the wavelength. Applying V_a to the actuator, the generated P-wave can read

$$u_a = \kappa_a V_a e^{ik_p y} \tag{5}$$

where κ_a denotes the electromechanical coupling coefficient of the piezoelectric actuator. Its value can be determined through a numerical test by calculating the displacement wave field with the actuator applied by an unit voltage. In the presence of V_a, the total wave field propagating away from the meta-boundary becomes

$$u_r = u_r^{(p)} + u_a = (U_0 + \kappa_a V_a) e^{ik_p y} \tag{6}$$

As discussed before, the sensing signal contains components of not only the incident and reflected P-waves but also the feedback effects due to the actuation, which is then written by

$$V_s = \kappa_s U_0 + G V_a \tag{7}$$

where κ_s denotes the electromechanical coupling coefficient of the piezoelectric sensor and G represents the feedback coefficient from actuating to sensing signals. In particular, the value of κ_s can also be numerically determined by calculating the sensing voltage through impinging an incident P-wave of unit displacement amplitude. On the other hand, by prohibiting incident waves and applying a voltage on the actuator, the ratio calculated numerically between sensing and actuating voltages defines G. By substituting Eq. (7) into the transfer function defined as, $H = V_a/V_s$, we have

$$H = \frac{\frac{V_a}{U_0}}{\kappa_s + G\frac{V_a}{U_0}} \tag{8}$$

On the other hand, by substituting Eqs. (3) and (6) into the reflection coefficient $r = u_r(y=0)/u_i(y=0)$, we obtain

$$r = 1 + \kappa_a \frac{V_a}{U_0} \tag{9}$$

Comparing Eqs. (8) and (9) and eliminating the term, V_a/U_0, the transfer function can be expressed as

$$H = \frac{r-1}{\kappa_s \kappa_a + G(r-1)} \tag{10}$$

Eq. (10) represents the relation between wave reflection coefficient and electrical transfer function. Therefore, the meta-boundary offers a way to tailor the reflection coefficient of P-waves locally along the plate boundary through programming the transfer function, H. According to Eq. (10), for a desired wave reflection coefficient, we can calculate the required electrical transfer function, or vice versa. Note that the transfer function H is derived from harmonic analysis at discrete frequencies. Therefore, causality and stability cannot be guaranteed over a range of frequencies, which should be carefully considered in experiments.

Table 1
Geometric parameters of the reprogrammable piezoelectric meta-boundary.

L	300 mm	w	10 mm	w_1	5 mm	h	3 mm
L_s	4 mm	L_1	3 mm	h_{p1}	0.2 mm	h_{p2}	1 mm
h_b	0.5 mm	h_g	0.5 mm				

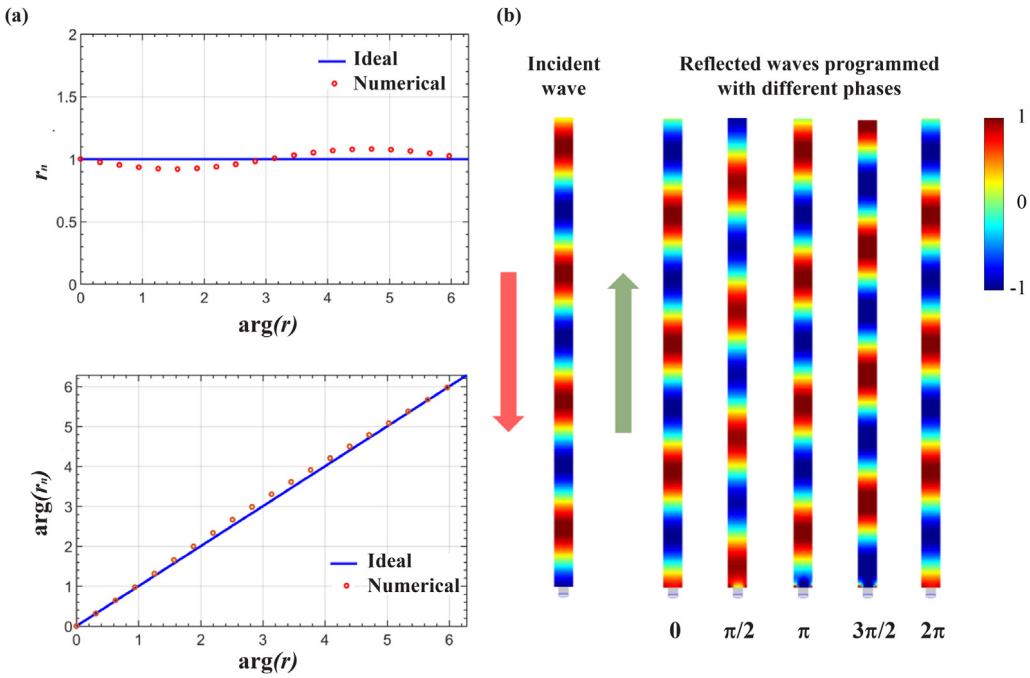

Fig. 3. (a) Numerically calculated amplitudes and phase angles of the reflection coefficient, r_n, by prescribing r with different phase angles in Eq. (8); (b) Normalized displacement wave fields of incident and reflected waves along y-direction for $\arg(r) = 0, \pi/2, \pi, 3\pi/2$ and 2π.

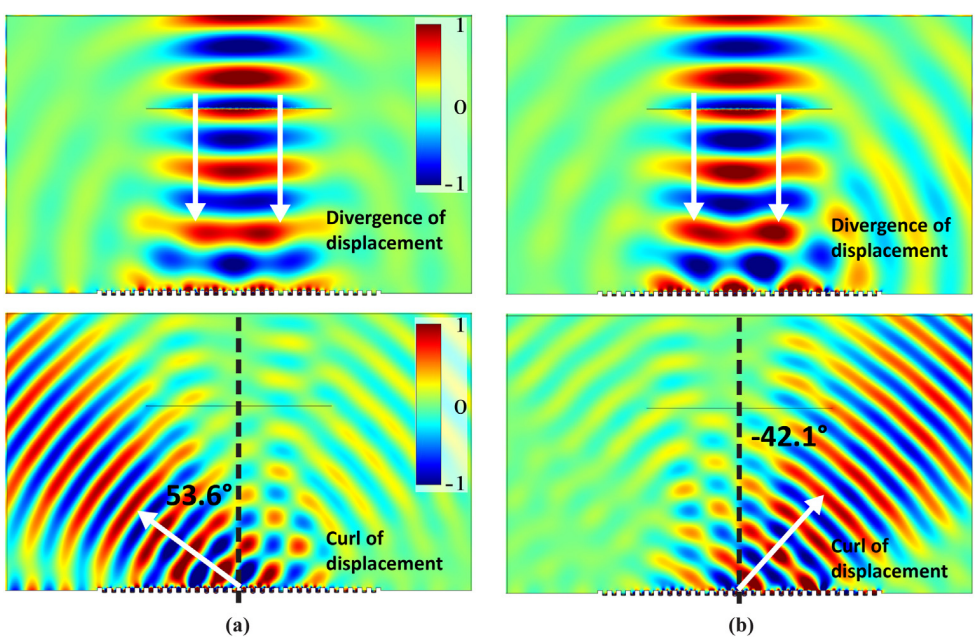

Fig. 4. Normalized divergence (top) and curl (bottom) of displacement wave fields under normal incidences: (a) $\frac{\Delta\phi}{\Delta x} = \pi/25$ rad/mm; (b) and $\frac{\Delta\phi}{\Delta x} = -\pi/30$ rad/mm.

3. Results

3.1. Phase manipulations in 1D setting

To validate the phase manipulation ability of the meta-boundary, piezoelectric coupled numerical simulations are performed using a commercial finite element software, COMSOL Multiphysics. In simulations, we apply the geometric setting shown in Fig. 2b and add a perfectly-matched layer to the other end of the rod to suppress reflected waves from that boundary. Plane stress assumptions are adopted in calculations, and geometric and material parameters are given in Tables 1 and 2, respectively. The transfer function, H, is implemented into the numerical model following Eq. (10). During calculations, our attention is paid on the cases only with phase modulations, such that $|r| = 1$. We select the operation frequency as 80 kHz, which can also be designed at different frequencies as well. Fig. 3a shows numerically calculated amplitudes and phase angles of the reflection coefficient, r_n, by prescribing r with different phase

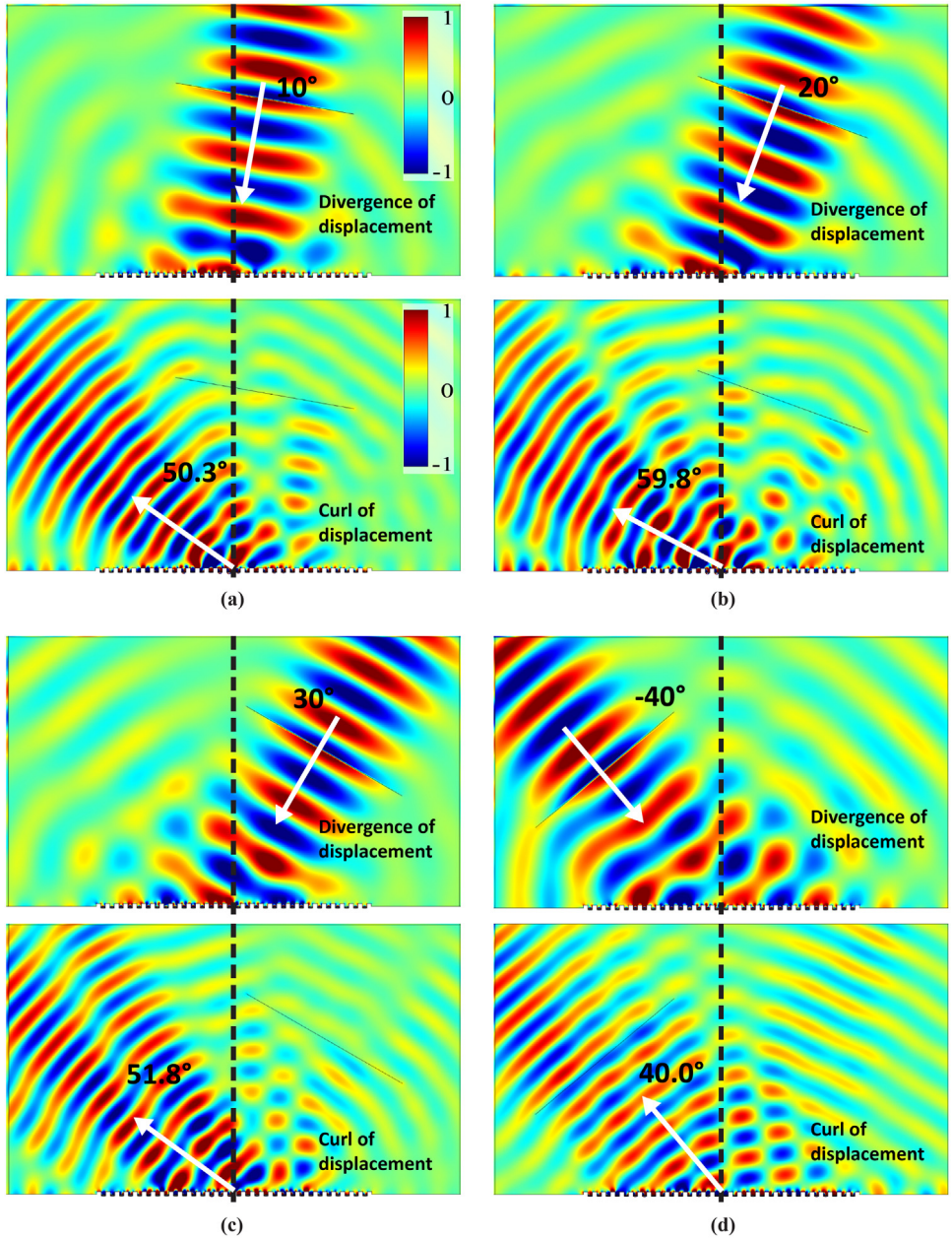

Fig. 5. Normalized divergence (top) and curl (bottom) of displacement wave fields under oblique incidences: (a) $\theta = 10°$, $\frac{\Delta\phi}{\Delta x} = \pi/30$ rad/mm; (b) $\theta = 20°$, $\frac{\Delta\phi}{\Delta x} = \pi/30$ rad/mm; (c) $\theta = 30°$, $\frac{\Delta\phi}{\Delta x} = \pi/40$ rad/mm; (d) $\theta = -40°$, $\frac{\Delta\phi}{\Delta x} = \pi/20$ rad/mm.

Table 2
Material properties of the reprogrammable piezoelectric meta-boundary.

Material properties (Steel)					
c_p	5700 $\mathrm{ms^{-1}}$	c_s	3220 $\mathrm{ms^{-1}}$	ρ_b	7850.0 $\mathrm{kg\,m^{-3}}$
Material properties (PZT 5H)					
s^E_{11}	16.5×10^{-12} $\mathrm{m^2N^{-1}}$	d_{33}	5.93×10^{-10} $\mathrm{CN^{-1}}$		
s^E_{33}	20.7×10^{-12} $\mathrm{m^2N^{-1}}$	d_{31}	-2.74×10^{-10} $\mathrm{CN^{-1}}$		
s^E_{44}	43.5×10^{-12} $\mathrm{m^2N^{-1}}$	d_{15}	7.41×10^{-10} $\mathrm{CN^{-1}}$		
s^E_{12}	-4.78×10^{-12} $\mathrm{m^2N^{-1}}$	ε^S_{33}	$1433.6\,\varepsilon_0$		
s^E_{13}	-8.45×10^{-12} $\mathrm{m^2N^{-1}}$	ε^S_{11}	$1704.4\,\varepsilon_0$		
ρ_p	7500.0 $\mathrm{kg\,m^{-3}}$	ε_0	8.842×10^{-12} $\mathrm{CmV^{-1}}$		

angles in Eq. (10). As illustrated in the figure, amplitudes of r_n almost remains around unitary with different phases in r and the calculated phase angles are very close to the prescribed ones, which is pursued to be achieved. This indicates that the meta-boundary is a good candidate for phase manipulations. As several phase manipulation cases, displacement wave fields of incident and reflected waves along y-direction are shown in Fig. 3b. The phase tuning effect is clearly seen from the figure for $\arg(r) = 0, \pi/2, \pi, 3\pi/2$ and 2π, respectively.

3.2. Shaping P- to S-wave conversions in a plate

We then construct a piezoelectric-based programmable meta-boundary with 30 unit cells to exploit its performances in controlling P- to S-wave conversions. Plane stress assumptions are applied again and the operation frequency is still at 80 kHz. Material and geometric parameters are the same as those used in Fig. 3. Perfectly-matched layers are implemented to the other three boundaries of the plate to inhibit boundary reflections. We apply

normal forces in a Gaussian profile on a line source to generate incident P-waves propagating to the meta-boundary. In the study, we focus on linear phase profiles of the reflection coefficient along the meta-boundary such that $\frac{\Delta\phi}{\Delta x}$ becomes a constant. We first examine the wave conversion performances under normal incidences, for which the conversion is considered to be vanished on a flat free boundary. Divergence of displacement denotes changes in volume and thus can display longitudinal or pressure (P-) wave propagation. On the other hand, curl of displacement represents infinitesimal rotation with no volume change and thus can display rotational or shear (S-) wave propagation. The divergence and curl of displacement fields are plotted to show the longitudinal and shear wave propagations. Figs. 4a and 4b show the normalized divergence and curl of the displacement wave fields with $\frac{\Delta\phi}{\Delta x} = \pi/25$ rad/mm and $-\pi/30$ rad/mm, respectively. As can be found from figures of the divergence of displacement wave fields, the reflected P-waves are very weak, as the wave field is almost antisymmetric with respect to the line source. In Fig. 4a, it is noticed that small amount of S-wave energy leaks to the negative direction due to higher-order diffraction. Rayleigh wave propagated to the left is also observed on the boundary, which is caused by the meta-boundary grating. However, compared with displacement fields in Fig. 4a, the amplitude of the reflected P-waves in Fig. 4b becomes slightly larger, which is caused by the higher-order diffraction, and in contrast the amplitude of the reflected S-wave becomes smaller. Although a diffracted P-wave is visible in Fig. 4b, its amplitude is quite small compared with the incident P-wave. Therefore, the P-wave is nearly totally converted to S-wave. Most importantly, the distributions of S-waves can be flexibly tailored, to the left or right side depending on the sign of the phase gradient, $\frac{\Delta\phi}{\Delta x}$ programmed in the meta-boundary (Fig. 4a and b). We quantitatively calculate reflection angles of the two cases based on Eq. (2), and find $\theta_2' = 53.6°$ and $-42.1°$, respectively, of which the directions are plotted by white arrows in figures of the curl of displacement fields. Good agreement between numerical results and analytical predictions is clearly seen. In contrast to normal incidences, the meta-boundary can also be operated for total wave mode conversions when incidences become oblique. To demonstrate these, Figs. 5a–5d show the normalized divergence and curl of displacement wave fields with $\theta = 10°$, $20°$, $30°$ and $-40°$, respectively. In Fig. 5a and b, $\frac{\Delta\phi}{\Delta x} = \pi/30$ rad/mm, incident P-waves are nearly totally converted to S-waves, which, at the same, are steered to predefined directions. We also notice that the total wave conversion is still not perfect for these two cases, especially in the near field, which may be caused by high-order diffraction. By programming $\frac{\Delta\phi}{\Delta x} = \pi/40$ rad/mm (Fig. 5c), total wave mode conversions still occur with $\theta = 30°$. Whereas, when $\theta = -40°$, the meta-boundary will no longer fully convert P-waves to S-waves with $\frac{\Delta\phi}{\Delta x} = \pi/30$ rad/mm or $\pi/40$ rad/mm, as indicated in Eq. (2). To make the total wave mode conversion possible, $\frac{\Delta\phi}{\Delta x}$ needs to be either negative or larger positive values. For each phase gradient discussed in Fig. 5a–c, there exists a critical angle θ_c and total wave mode conversion is expected if incidence angles are larger than θ_c. It is also important to mention that the meta-boundary can be reconfigurable to realize the total wave conversion at other frequencies by redesigning the electrical transfer function, H. The meta-boundary proposed can be easily scaled up or down for various wave mode converting applications. In Fig. 5d, we select $\frac{\Delta\phi}{\Delta x} = \pi/20$ rad/mm, and find the converted S-wave propagates back to the incident direction. The meta-boundary therefore functions as a "retroreflector", where the incident and reflected waves have different polarizations.

4. Conclusion

In conclusion, we introduce a piezoelectric-based meta-boundary controlled by electrical circuits to disturb, in a reprogrammed way, P- and S-wave conversions on a free boundary. The meta-boundary is designed by building an array of piezoelectric sensing-and-actuating units connected by feedback control loops. Using numerical simulations, we demonstrate the meta-boundary supports total wave mode conversions, from P- to S-waves in particular. The programmability of electrical control circuits allows converted S-waves to be steered to different directions, and incident waves spanning a large range of angles. We believe the piezoelectric-based programmable meta-boundary suggested herein could shed light in the design of elastodynamic control devices in general, and in non-destructive evaluation, medical ultrasonics and imaging, protection of underwater structures and acoustic cloaks in particular.

Declaration of competing interest

The authors declare that they have no known competing financial interests or personal relationships that could have appeared to influence the work reported in this paper.

Acknowledgments

This work is supported by the Air Force Office of Scientific Research under Grant No. AF 9550-18-1-0342 with Program Manager Dr. Byung-Lip (Les) Lee.

References

[1] K.F. Graff, Wave Motion in Elastic Solids, Courier Corporation, 2012.
[2] X. Su, Z. Lu, A.N. Norris, Elastic metasurfaces for splitting SV-and P-waves in elastic solids, J. Appl. Phys. 123 (9) (2018) 091701.
[3] A. Climente, D. Torrent, J. Sánchez-Dehesa, Gradient index lenses for flexural waves based on thickness variations, Appl. Phys. Lett. 105 (6) (2014) 064101.
[4] M. Mitra, S. Gopalakrishnan, Guided wave based structural health monitoring: A review, Smart Mater. Struct. 25 (5) (2016) 053001.
[5] W.J. Staszewski, Structural health monitoring using guided ultrasonic waves, in: Advances in Smart Technologies in Structural Engineering, Springer, 2004, pp. 117–162.
[6] Y. Tian, Y. Shen, D. Rao, W. Xu, Metamaterial improved nonlinear ultrasonics for fatigue damage detection, Smart Mater. Struct. 28 (7) (2019) 075038.
[7] C.A. Chua, P. Cawley, Crack growth monitoring using fundamental shear horizontal guided waves, Struct. Health Monit. (2019) 1475921719882330.
[8] L.W. Schmerr, Fundamentals of Ultrasonic Nondestructive Evaluation, Springer, 2016.
[9] A.P. Sarvazyan, O.V. Rudenko, S.D. Swanson, J.B. Fowlkes, S.Y. Emelianov, Shear wave elasticity imaging: a new ultrasonic technology of medical diagnostics, Ultrasound Med. Biol. 24 (9) (1998) 1419–1435.
[10] R.M. Sturm, E.B. Yerkes, J.L. Nicholas, D. Snow-Lisy, D.D. Saldano, P.L. Gandor, C.G. Halline, I. Rosoklija, K. Rychlik, E.K. Johnson, et al., Ultrasound shear wave elastography: a novel method to evaluate bladder pressure, J. Urol. 198 (2) (2017) 422–429.
[11] J.L. Rose, Ultrasonic Guided Waves in Solid Media, Cambridge university press, 2014.
[12] R. Zhu, X. Liu, G. Hu, C. Sun, G. Huang, Negative refraction of elastic waves at the deep-subwavelength scale in a single-phase metamaterial, Nat. Commun. 5 (1) (2014) 1–8.
[13] J.M. Kweun, H.J. Lee, J.H. Oh, H.M. Seung, Y.Y. Kim, Transmodal Fabry-Pérot resonance: theory and realization with elastic metamaterials, Phys. Rev. Lett. 118 (20) (2017) 205901.
[14] H.J. Lee, J.-R. Lee, S.H. Moon, T.-J. Je, E.-c. Jeon, K. Kim, Y.Y. Kim, Off-centered double-slit metamaterial for elastic wave polarization anomaly, Sci. Rep. 7 (1) (2017) 1–13.
[15] M.S. Kim, W.R. Lee, Y.Y. Kim, J.H. Oh, Transmodal elastic metasurface for broad angle total mode conversion, Appl. Phys. Lett. 112 (24) (2018) 241905.
[16] C. Coulais, D. Sounas, A. Alù, Static non-reciprocity in mechanical metamaterials, Nature 542 (7642) (2017) 461–464.

[17] B. Florijn, C. Coulais, M. van Hecke, Programmable mechanical metamaterials, Phys. Rev. Lett. 113 (17) (2014) 175503.
[18] N. Correll, R. Voyles, Robotic materials: From smart polymers to computational metamaterials, in: Proc. Robot Makers Workshop, Robotics: Science Systems Conf., 2014.
[19] Y. Chen, G. Hu, G. Huang, An adaptive metamaterial beam with hybrid shunting circuits for extremely broadband control of flexural waves, Smart Mater. Struct. 25 (10) (2016) 105036.
[20] A.M. Baz, An active acoustic metamaterial with tunable effective density, J. Vib. Acoust. 132 (4) (2010).
[21] Z. Chen, C. Xue, L. Fan, S.-y. Zhang, X.-j. Li, H. Zhang, J. Ding, A tunable acoustic metamaterial with double-negativity driven by electromagnets, Sci. Rep. 6 (2016) 30254.
[22] Y. Chen, X. Li, H. Nassar, G. Hu, G. Huang, A programmable metasurface for real time control of broadband elastic rays, Smart Mater. Struct. 27 (11) (2018) 115011.
[23] Q. He, S. Sun, L. Zhou, et al., Tunable/reconfigurable metasurfaces: Physics and applications, Research 2019 (2019) 1849272.
[24] A. Minovich, D.N. Neshev, D.A. Powell, I.V. Shadrivov, Y.S. Kivshar, Tunable fishnet metamaterials infiltrated by liquid crystals, Appl. Phys. Lett. 96 (19) (2010) 193103.
[25] N.I. Zheludev, Y.S. Kivshar, From metamaterials to metadevices, Nat. Mater. 11 (11) (2012) 917–924.
[26] D. Yang, L. Jin, R.V. Martinez, K. Bertoldi, G.M. Whitesides, Z. Suo, Phase-transforming and switchable metamaterials, Extreme Mech. Lett. 6 (2016) 1–9.
[27] X. Zheng, H. Lee, T.H. Weisgraber, M. Shusteff, J. DeOtte, E.B. Duoss, J.D. Kuntz, M.M. Biener, Q. Ge, J.A. Jackson, et al., Ultralight, ultrastiff mechanical metamaterials, Science 344 (6190) (2014) 1373–1377.
[28] X. Li, Y. Chen, G. Hu, G. Huang, A self-adaptive metamaterial beam with digitally controlled resonators for subwavelength broadband flexural wave attenuation, Smart Mater. Struct. 27 (4) (2018) 045015.
[29] S. Li, J. Xu, J. Tang, Tunable modulation of refracted lamb wave front facilitated by adaptive elastic metasurfaces, Appl. Phys. Lett. 112 (2) (2018) 021903.
[30] B.-I. Popa, D. Shinde, A. Konneker, S.A. Cummer, Active acoustic metamaterials reconfigurable in real time, Phys. Rev. B 91 (22) (2015) 220303.
[31] K. Yi, M. Ouisse, E. Sadoulet-Reboul, G. Matten, Active metamaterials with broadband controllable stiffness for tunable band gaps and non-reciprocal wave propagation, Smart Mater. Struct. 28 (6) (2019) 065025.
[32] F. Casadei, M. Ruzzene, L. Dozio, K. Cunefare, Broadband vibration control through periodic arrays of resonant shunts: experimental investigation on plates, Smart Mater. Struct. 19 (1) (2009) 015002.
[33] Y. Chen, R. Zhu, M. Barnhart, G. Huang, Enhanced flexural wave sensing by adaptive gradient-index metamaterials, Sci. Rep. 6 (2016) 35048.
[34] C. Sugino, A. Erturk, Analysis of multifunctional piezoelectric metastructures for low-frequency bandgap formation and energy harvesting, J. Phys. D: Appl. Phys. 51 (21) (2018) 215103.